

Metallic liquid H₃O in a thin-shell zone inside Uranus and Neptune

Peihao Huang^{1†}, Hanyu Liu^{1†}, Jian Lv¹, Quan Li^{1,4}, Chunhong Long², Yanchao Wang^{1*}, Changfeng Chen^{3*}, Yanming Ma^{1,4*}

¹State Key Laboratory of Superhard Materials & Innovation Center for Computational Physics Methods and Software, College of Physics, Jilin University, Changchun 130012, China.

²Beijing Computational Science Research Center, Beijing 100193, China.

³Department of Physics and Astronomy, University of Nevada, Las Vegas, Nevada 89154, United States.

⁴International Center of Future Science, Jilin University, Changchun 130012, China.

†These authors contributed equally to this work

The Solar System harbors deep unresolved mysteries despite centuries-long study. A highly intriguing case concerns anomalous non-dipolar and non-axisymmetric magnetic fields of Uranus and Neptune that have long eluded explanation by the prevailing theory. A thin-shell dynamo conjecture captures observed phenomena but leaves unexplained fundamental material basis and underlying mechanism. Here, we report the discovery of trihydrogen oxide (H₃O) in metallic liquid state stabilized at extreme pressure and temperature conditions inside these icy planets. Calculated stability pressure field compared to known pressure-radius relation for Uranus and Neptune places metallic liquid H₃O in a thin-shell zone near planetary cores. These findings from accurate quantum mechanical calculations rationalize the empirically conjectured thin-shell dynamo model and establish key physical benchmarks that are essential to elucidating the enigmatic magnetic-field anomaly of Uranus and Neptune, resolving a major mystery in planetary science.

Planetary magnetic fields are commonly attributed to the magnetohydrodynamic dynamo. Earth's geomagnetic field is generated in a thick layer of fluid iron outer core, and the magnetic fields of Jupiter and Saturn are produced by their respective thick layers of metallic fluid hydrogen. Magnetic fields of most planets in the Solar System are axial-dipole dominated, except for Uranus and Neptune that exhibit anomalous non-dipolar and non-axisymmetric fields. This intriguing phenomenon raises fundamental questions about the physics mechanism and underlying material foundation.

Uranus and Neptune each contain three constituent regions¹, namely a gaseous

hydrogen-helium atmosphere, a thick intermediate layer of “hot ices”, and a rocky core. The pressure and temperature in their atmospheres are insufficient to produce metallic hydrogen^{2,3}, and iron in their cores is probably in solid state^{3,4} and thus inconsequential in the dynamo model. The middle “ice layer” is therefore the most likely place to generate magnetic fields. This layer is estimated to possess 56% H₂O, 36% CH₄, and 8% NH₃ in molar fractions⁵, and its pressure and temperature conditions range from 20 to 600 GPa and 2,000 to 7,000 K, respectively. The H₂O in the form of superionic ice may constitute a large fraction of the ice layer⁵⁻⁸ and ionic fluid water exists in the remaining outer part of the ice layer. The conductivity of the ionic ice, estimated to be 2 to 20 ($\Omega \text{ cm}$)⁻¹, is too small to generate the magnetic fields in Uranus and Neptune^{9,10}. The conductivity of the superionic ice is near 100 ($\Omega \text{ cm}$)⁻¹, which is still too small and need to be compensated by vigorous convection with flow velocities similar to those stirring Earth’s liquid outer core ($\sim 100 \text{ m yr}^{-1}$) to sustain a dynamo in a superionic ice layer, but the requirements for this scenario are considered unrealistic⁷.

It is known that CH₄ becomes unstable and dissociates into C and H₂ above 10 GPa and 2,000 K¹¹⁻¹⁴, and NH₃ reacts with water to produce molecular mixtures in the form of (H₂O)(NH₃)₂¹⁵ from 79 to 540 GPa. Given the estimated molar fractions of H₂O, CH₄, and NH₃ in their ice layers⁵, the mantle regions of these planets are expected to host a hydrogen-rich environment with the H₂O:H₂ ratio reaching 13:18 assuming full dissociation of CH₄ and complete mixing of NH₃ with H₂O in a ratio of 2:1.

Past studies examined miscibility of H₂ and H₂O in pressure and temperature ranges of 2-70 GPa and 1,000-6,000 K, respectively,¹⁶ which do not correspond to conditions deep inside Uranus and Neptune. It remains a viable prospect that H₂ could react with H₂O, which is the most abundant component in the ice layer of these planets, to produce new compounds that may provide the material basis for generating magnetic fields.

We examined H₂-H₂O systems using an inhouse material structure search method^{17,18}. Our search uncovered trihydrogen oxide (H₃O) that is stable at 600 GPa (Fig. 1a). This stoichiometry was previously reported but at much higher pressures ($\sim 14 \text{ TPa}$)¹⁹. The unit cell of H₃O contains 64 atoms, and its hydrogen-oxygen covalent framework has a

H:O ratio of 2:1, with remaining hydrogen in the voids in the form of H₂ molecules. The basic structural unit hosts six distinct bond lengths and three different bond angles (Fig. 1c). Adjacent basic units are nested, and the unit cell contains 4 basic units. The bond length in the H₂ unit is 0.65 Å at 500 GPa, which is much shorter than that in solid hydrogen at ambient pressure (0.74 Å). Further assessments of formation enthalpy show that H₃O is stable against decomposition to H₂O and H₂ above 450 GPa (Fig. 1b).

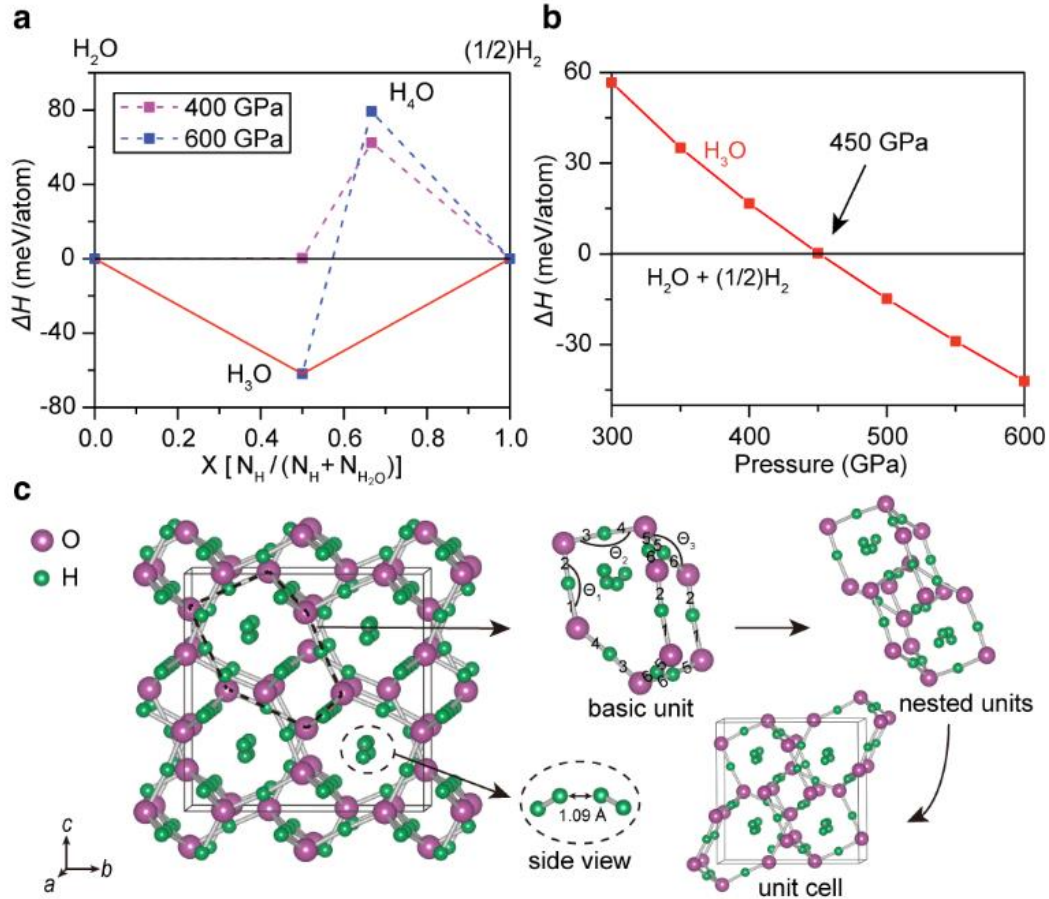


Fig. 1 | Formation enthalpy and crystal structure of H₃O. **a**, Formation enthalpy of H-O compounds with respect to decomposition into H₂O and H₂ at 400 and 600 GPa. **b**, Enthalpy including the effect of zero-point energy versus pressure for H₃O relative to the results for decomposed H₂O and H₂. **c**, Crystal structure (space group *Cmca*) and basic structural units of H₃O. Lattice parameters at 500 GPa are $a=3.35$ Å, $b=5.84$ Å, and $c=5.80$ Å. There are two inequivalent atomic positions for O and four for H: O1 at 8f (0.00, 0.16, 0.00) and O2 at 8f (0.50, 0.49, 0.34), H1 at 8f (0.00, 0.33, 0.07), H2 at 8f (0.00, 0.43, 0.34), H3 at 16g (0.76, 0.09, 0.09) and H4 at 16g (0.33, 0.24, 0.23). Six distinct bonds in the basic unit labeled 1 through 6 have lengths 1.16, 1.02, 1.08, 1.06, 1.06 and 1.10 Å, respectively, and three bond angles $\theta_1=174.58^\circ$, $\theta_2=174.67^\circ$ and $\theta_3=171.33^\circ$. Adjacent basic units are nested to form the unit cell of the H₃O crystal.

The stability pressure field of 450-600 GPa for H₃O lies within the pressure range of 20-600 GPa in the interiors of Uranus and Neptune, which also host high temperatures. We examined pertinent pressure-temperature phase diagram using *ab initio* molecular dynamics (AIMD) simulations. Fig. 2 shows simulated mean square displacement (MSD) and trajectory of H₃O at the density of 4.30 g/cm³. At 1,000 K, MSD values of hydrogen and oxygen atoms remain nearly constant (Fig. 2a), showing the system in a stable solid state with all atoms near equilibrium positions (Fig. 2d). At 3,000 K, MSD values for hydrogen atoms begin to increase, but values for oxygen atoms remain nearly constant (Fig. 2b), signaling a transition into superionic state, corroborated by trajectory data (Fig. 2e) showing that oxygen atoms remain near their equilibrium positions while hydrogen atoms diffuse. At further increased temperature (6,000 K), oxygen atoms also diffuse (Fig. 2c and 2f). Systematic calculations show that H₃O transforms from solid to superionic state at 1,250 K at 4.30 g/cm³, then to liquid state at 5,250 K (see Fig. 3).

We also ran simulations for H₂O at the density of 4.93 g/cm³ and temperatures of 5,000-8,000 K, with the equilibrium pressure (~600 GPa) close to that for H₃O at 4.30 g/cm³ and 7,000 K. We find that H₂O remains in a superionic state up to 7,000 K, where H₃O enters a liquid state. We performed AIMD simulations using a supercell (Extended Data Fig. 1a) containing 144 atoms in the *Pbcm*-H₂O²⁰ structure and 48 atoms in the *I4₁/amd*-H structure²¹ in the simulation box at 4.30 g/cm³ and 7,000 K. The results show that hydrogen atoms can easily penetrate into the H₂O lattice (Extended Data Fig. 1b), and the radial distribution function of the H-H₂O mix matches that of H₃O (Extended Data Fig. 1c). These results validate the scenario of H₂O reacting with H to form liquid H₃O at such extreme planetary pressure and temperature conditions.

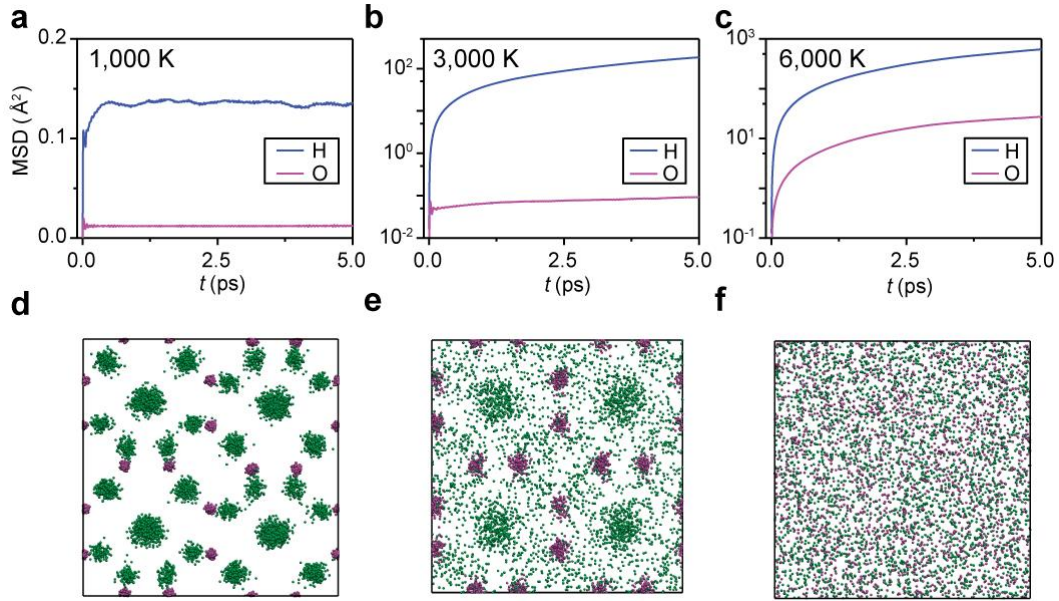


Fig. 2 | Simulation of solid, superionic and liquid phase of H₃O. **a-c**, Mean square displacement of oxygen and hydrogen in H₃O at **(a)** 1,000 K, **(b)** 3,000 K, and **(c)** 6,000 K at the density of 4.30 g/cm³, in solid, superionic and liquid phases. **d-f**, Trajectory snapshots of the corresponding phases of H₃O, where purple and green spheres represent instantaneous positions of oxygen and hydrogen atoms, respectively.

We have constructed the pressure-temperature phase diagram of H₃O covering the conditions corresponding to the interiors of Uranus and Neptune (Fig. 3a). Phase boundaries (dashed lines) separating the solid, superionic and liquid states are determined by AIMD simulations. The boundary separating H₃O and its decomposition compounds (H₂O and H₂) at low temperatures (red open symbols) is determined by the difference of Gibbs free energy estimated using the quasi-harmonic approximation²². The isentropes of Uranus and Neptune pass through regions of the liquid phase of H₃O above ~518 GPa, indicating that liquid H₃O is viable deep inside these icy giants surrounding their rocky cores. From an estimated pressure-radius relationship for these planets²³, liquid H₃O can stably exist in a thin-shell zone between 0.32 R to 0.38 R from the planetary center (Fig. 3b), where R is the total radius of the planet.

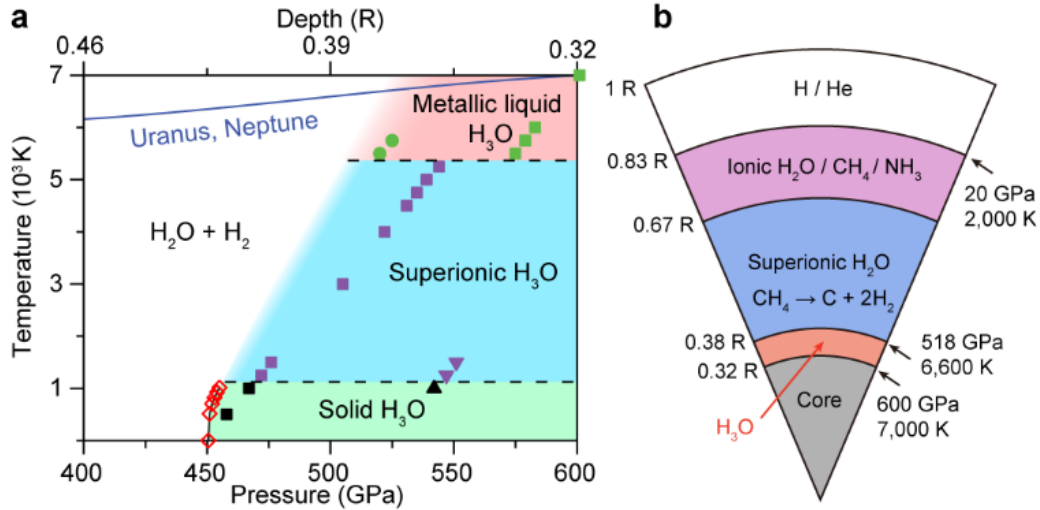


Fig. 3 | The pressure-temperature phase diagram of H₃O and its presence in a thin-shell zone inside Uranus and Neptune. **a**, Stability fields separating H₂O+H₂ and solid, superionic, and metallic liquid phases of H₃O, obtained from AIMD simulations. The blue solid line is the isentrope of Neptune or Uranus²⁴. Data points in filled circles, filled squares and filled triangles are AIMD simulation results at 4.14, 4.30 and 4.52 g/cm³, respectively. **b**, Schematic of planetary interior structure of Uranus and Neptune. The grey and white regions represent the core and outer gas layer, respectively. The purple, blue and orange areas represent regions dominated by ionic H₂O, superionic H₂O and liquid H₃O, respectively. The pressure-radius relation is extracted from the estimate by Ravit Helled *et al.*²³.

Electrical conductivity is crucial to understanding planetary magnetic fields in the dynamo theory. Our electronic bandgap calculations show that H₃O has much lower metallization temperature (~5,000 K at 539 GPa) compared to H₂O (~6,000 K at 587 GPa) (Extended Data Fig. 2a). This result indicates that H₃O turns into a metallic liquid in deep mantle regions of Uranus and Neptune; meanwhile, H₂O remains superionic and does not turn into a metallic liquid at the highest temperature and pressure conditions (7,000 K and 600 GPa) in the ice layer of these planets. Calculated direct current (DC) electrical conductivity results (Extended Data Fig. 2b) show an abrupt increase of conductivity between 5,000 and 6,000 K for H₃O, from 19 to 164 (Ωcm)⁻¹, which is consistent with the bandgap results. Meanwhile, electrical conductivity of H₂O shows no sudden change, and is an order of magnitude lower than that of H₃O above 6,000 K (Extended Data Fig. 2b). The metallization of H₃O may be attributed to a similar mechanism underlying melting-prompted conduction in diamond²⁵ and N₂²⁶.

A conjectured new planetary structural model^{27,28} is able to reproduce the unusual magnetic fields of Uranus and Neptune in the context of the dynamo theory. The central component of this model is a thin shell of electrically conducting fluid, in contrast to thick rotating shells in other planets possessing magnetic fields. The present study predicts a narrow radial range for H₂O phase stability in deep mantle regions of Uranus and Neptune, providing compelling evidence for the conjectured thin-shell structure^{27,28}. Moreover, fluids with high electrical conductivity are essential to generating planetary magnetic fields²⁹. Our calculations reveal that electrical conductivity of H₂O reaches 164 (Ωcm)⁻¹ at 6,000 K, an order of magnitude larger than the conductivity of ~20 (Ωcm)⁻¹ for ionic ice, which was previously proposed to be responsible for the magnetic field of Uranus³⁰. Liquid H₂O is also more prone to convection than superionic ice, whose viscosity is several orders of magnitude larger than that of typical fluids, making H₂O more conducive to producing magnetic fields. The present findings provide crucial foundation for resolving the magnetic-field anomaly of Uranus and Neptune, and the insights may prove useful in exploring pertinent phenomena in giant icy exo-planets.

- 1 Hubbard, W. B. & MacFarlane, J. J. Structure and evolution of Uranus and Neptune. *J. Geophys. Res.-Solid Earth* **85**, 225-234 (1980).
- 2 Ness, N. F. *et al.* Magnetic fields at Uranus. *Science* **233**, 85-89 (1986).
- 3 De Pater, I. & Lissauer, J. J. *Planetary sciences*. (Cambridge University Press, 2015).
- 4 Jones, C. A. Planetary magnetic fields and fluid dynamos. *Annu. Rev. Fluid Mech.* **43**, 583-614 (2011).
- 5 Cavazzoni, C. *et al.* Superionic and metallic states of water and ammonia at giant planet conditions. *Science* **283**, 44-46 (1999).
- 6 Wilson, H. F., Wong, M. L. & Militzer, B. Superionic to superionic phase change in water: consequences for the interiors of Uranus and Neptune. *Phys. Rev. Lett.* **110**, 151102 (2013).
- 7 Millot, M. *et al.* Experimental evidence for superionic water ice using shock compression. *Nat. Phys.* **14**, 297-302 (2018).
- 8 Millot, M. *et al.* Nanosecond X-ray diffraction of shock-compressed superionic water ice. *Nature* **569**, 251-255 (2019).
- 9 Ness, N. F. *et al.* Magnetic fields at Neptune. *Science* **246**, 1473-1478 (1989).
- 10 Stevenson, D. J. Planetary magnetic fields: achievements and prospects. *Space Sci. Rev.* **152**, 651-664 (2010).
- 11 Benedetti, L. R. *et al.* Dissociation of CH₄ at high pressures and temperatures: diamond formation in giant planet interiors? *Science* **286**, 100-102 (1999).
- 12 Gao, G. *et al.* Dissociation of methane under high pressure. *J. Chem. Phys.* **133**, 144508 (2010).

- 13 Kraus, D. *et al.* Formation of diamonds in laser-compressed hydrocarbons at planetary interior conditions. *Nat. Astron.* **1**, 606-611 (2017).
- 14 Ross, M. The ice layer in Uranus and Neptune—diamonds in the sky? *Nature* **292**, 435-436 (1981).
- 15 Robinson, V. N., Marqués, M., Wang, Y., Ma, Y. & Hermann, A. Novel phases in ammonia-water mixtures under pressure. *J. Chem. Phys.* **149**, 234501 (2018).
- 16 Soubiran, F. & Militzer, B. Miscibility calculations for water and hydrogen in giant planets. *Astrophys. J.* **806**, 228 (2015).
- 17 Wang, Y., Lv, J., Zhu, L. & Ma, Y. CALYPSO: A method for crystal structure prediction. *Comput. Phys. Commun.* **183**, 2063-2070 (2012).
- 18 Wang, Y., Lv, J., Zhu, L. & Ma, Y. Crystal structure prediction via particle-swarm optimization. *Phys. Rev. B* **82**, 094116 (2010).
- 19 Zhang, S., Wilson, H. F., Driver, K. P. & Militzer, B. H₂O and other hydrogen-oxygen compounds at giant-planet core pressures. *Phys. Rev. B* **87**, 024112 (2013).
- 20 Benoit, M., Bernasconi, M., Focher, P. & Parrinello, M. New high-pressure phase of ice. *Phys. Rev. Lett.* **76**, 2934-2936 (1996).
- 21 McMahon, J. M. & Ceperley, D. M. Ground-state structures of atomic metallic hydrogen. *Phys. Rev. Lett.* **106**, 165302 (2011).
- 22 Togo, A., Oba, F. & Tanaka, I. First-principles calculations of the ferroelastic transition between rutile-type and CaCl₂-type SiO₂ at high pressures. *Phys. Rev. B* **78**, 134106 (2008).
- 23 Helled, R., Anderson, J. D., Podolak, M. & Schubert, G. Interior models of Uranus and Neptune. *Astrophys. J.* **726**, 15 (2010).
- 24 Hubbard, W., Podolak, M. & Stevenson, D. The interior of Neptune. *Neptune and Triton* **109** (1995).
- 25 Eggert, J. H. *et al.* Melting temperature of diamond at ultrahigh pressure. *Nat. Phys.* **6**, 40 (2009).
- 26 Jiang, S. *et al.* Metallization and molecular dissociation of dense fluid nitrogen. *Nat. Commun.* **9**, 2624 (2018).
- 27 Stanley, S. & Bloxham, J. Convective-region geometry as the cause of Uranus' and Neptune's unusual magnetic fields. *Nature* **428**, 151-153 (2004).
- 28 Stanley, S. & Bloxham, J. Numerical dynamo models of Uranus' and Neptune's magnetic fields. *Icarus* **184**, 556-572 (2006).
- 29 Nellis, W. J. The unusual magnetic fields of Uranus and Neptune. *Mod. Phys. Lett. B* **29**, 1430018 (2015).
- 30 Nellis, W. J. *et al.* The nature of the interior of Uranus based on studies of planetary ices at high dynamic pressure. *Science* **240**, 779-781 (1988).

Acknowledgements We acknowledge funding from the National Natural Science Foundation of China (Grant No. 11822404, 11774127, 11534003 and 11622432), the National Key Research and Development Program of China under Grant No. 2016YFB0201200, No. 2016YFB0201201, and No. 2017YFB0701503, Science Challenge Project No. TZ2016001, and Program for JLU Science and Technology Innovative Research Team (JLUSTIRT). We utilized computing facilities at the High Performance Computing Center of Jilin University and Tianhe2-JK at the Beijing Computational Science Research Center.

Author Contributions Y.M. and Y.W. conceived and designed the project. Y.W. predicted the H₃O structure. P.H. performed simulations. P.H., H.L., Y.W., Y. M., C.C., J.L. and Q.L. performed data analysis. All authors wrote the manuscript and contributed to discussions of the results and revision of the manuscript.

Competing Interests The authors declare no competing interests.

Materials & Correspondence Correspondence and requests for materials should be addressed to Y.W. (wyc@calypso.cn), C.C. (chen@physics.unlv.edu), and Y.M. (mym@calypso.cn; mym@jlu.edu.cn).

Methods

We have performed extensive structure searches through a swarm-intelligence-based CALYPSO method and its same-name code, which enables global structure searching in conjunction with *ab initio* energetic calculations. This method has been benchmarked on various known systems.³¹⁻³⁴ The DFT calculations are performed using the VASP plane-wave code^{35,36}, where the Perdew-Burke-Ernzerhof (PBE) generalized gradient approximation density functional³⁷ and frozen-core all-electron projector-augmented wave (PAW) potentials³⁸ are adopted. The cutoff radius of the pseudopotentials for oxygen and hydrogen are 0.58 Å and 0.42 Å, respectively. To ensure validity of the adopted pseudopotentials, we also performed full-potential all-electron calculations for the equation of states of H₃O over the pressure range studied here by using the WIEN2K code³⁹. The results of our VASP calculations are nearly identical to those obtained from all-electron calculations (Extended Data Fig. 3), validating the pseudopotentials up to 600 GPa. The electronic wave functions are expanded in a plane-wave basis set with a kinetic energy cutoff of 1,200 eV, and the Brillouin zone (BZ) sampling is performed on k-meshes with a reciprocal space resolution of $2\pi \times 0.032 \text{ \AA}^{-1}$ to ensure that energies are converged to 1 meV/atom. The phonon calculations are performed through the PHONOPY code⁴⁰ using a finite displacement approach⁴¹.

The AIMD simulations are performed in the canonical (NVT) ensemble applying a Nosé thermostat. A system containing 128 atoms is used for H₃O. Simulations reach 15 ps, with the first 2-5 ps for equilibrating the system. The time step is chosen to be 0.5 fs. A $2 \times 2 \times 2$ k-mesh grid is used for the BZ sampling. To check for size effect, a larger system with 576 atoms is adopted. The transition temperature of this larger system is the same as that of the smaller system, confirming convergence regarding system size. The simulated temperatures range from 1,000 to 7,000 K with a temperature step of 500 K, and we choose the temperature step in interested regions (1,000-1,500 K and 5,000-6,000 K) to be 250 K to investigate the phase-transition temperatures from solid to superionic phase, and then to liquid phase. The simulation cell of H₂O contains 144 atoms. The Gibbs free energy (G) is calculated via quasi-harmonic approximation by the PHONOPY code. Gibbs free energy is defined at a constant temperature (T) and

pressure (P) by the formula: $G(T, P) = \min_V [U(V) + PV + F_{\text{phonon}}(T, V)]$, where U is the internal lattice energy, V is volume and F_{phonon} is the phonon free energy. $F_{\text{phonon}}(T, V) = k_B T \int_0^\infty g(\omega, V) \ln[2 \sinh(\frac{\hbar\omega}{2k_B T})] d\omega$, where $g(\omega, V)$ is the phonon density of states at frequency ω and volume V. The minimal value of G is found at the equilibrium volume for a given T and P.

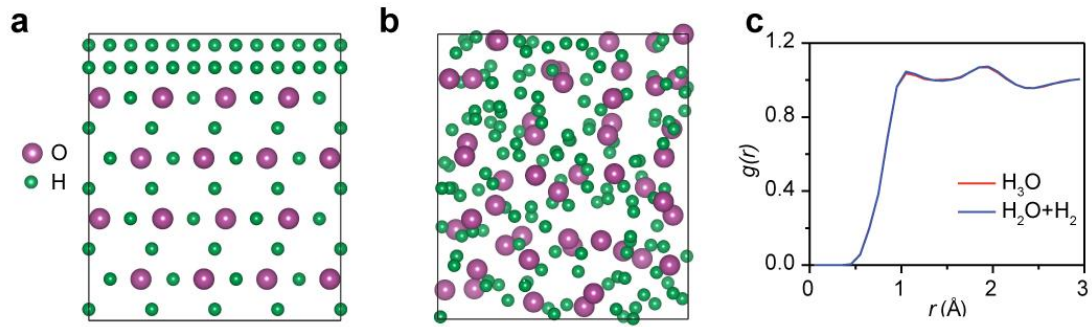
The time-averaged bandgap is calculated by the PBE functional (50 configurations for averaging) and cross checked using the GW methods (10 configurations for averaging). For GW calculations, a $2 \times 2 \times 2$ k-mesh grid is used for balancing accuracy and efficiency (Extended Data Fig. 4). Calculations show that the PBE and GW results are in good accordance, with consistent conclusion about H₃O reaching metallic state (Extended Data Fig. 5) under the same pressure and temperature conditions. The time-averaged DC electrical conductivity is calculated via the Kubo-greenwood formula^{42,43} using the KGEC code⁴⁴, which is a post-processor module for use with Quantum Espresso⁴⁵. To obtain converged conductivity results, 576 atoms for H₃O and 540 atoms for H₂O are used. A $3 \times 3 \times 3$ k-mesh is used for BZ sampling. Each conductivity result is evaluated by averaging over 10 configurations.

Data availability

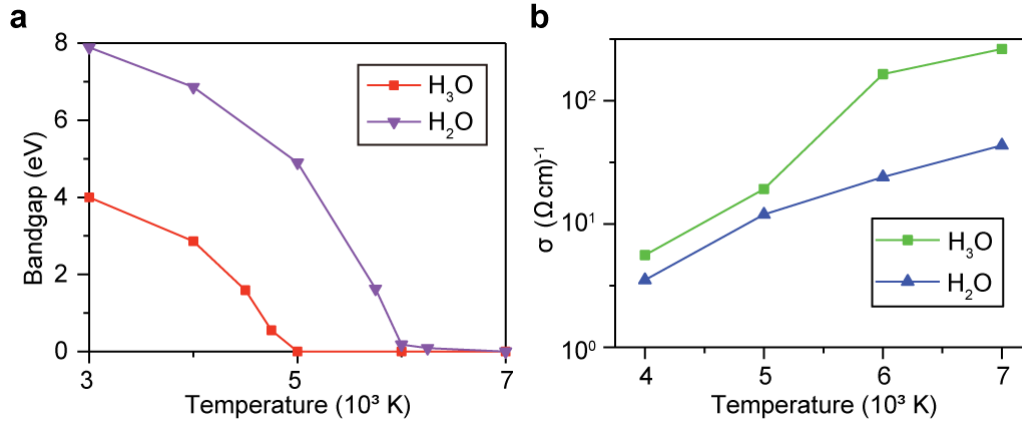
The data that support the findings of this study are available from the corresponding author upon reasonable requests.

- 31 Peng, F., Miao, M., Wang, H., Li, Q. & Ma, Y. Predicted lithium–boron compounds under high pressure. *J. Am. Chem. Soc.* **134**, 18599-18605 (2012).
- 32 Lv, J., Wang, Y., Zhu, L. & Ma, Y. Predicted novel high-pressure phases of lithium. *Phys. Rev. Lett.* **106**, 015503 (2011).
- 33 Zhu, L., Liu, H., Pickard, C. J., Zou, G. & Ma, Y. Reactions of xenon with iron and nickel are predicted in the Earth's inner core. *Nat. Chem.* **6**, 644 (2014).
- 34 Wang, H., Tse, J. S., Tanaka, K., Iitaka, T. & Ma, Y. Superconductive sodalite-like clathrate calcium hydride at high pressures. *Proc. Natl. Acad. Sci. U. S. A.* **109**, 6463-6466 (2012).
- 35 Kresse, G. & Furthmüller, J. Efficient iterative schemes for ab initio total-energy calculations using a plane-wave basis set. *Phys. Rev. B* **54**, 11169-11186 (1996).
- 36 Kresse, G. & Furthmüller, J. Efficiency of ab-initio total energy calculations for metals and semiconductors using a plane-wave basis set. *Comput. Mater. Sci.* **6**, 15-50 (1996).

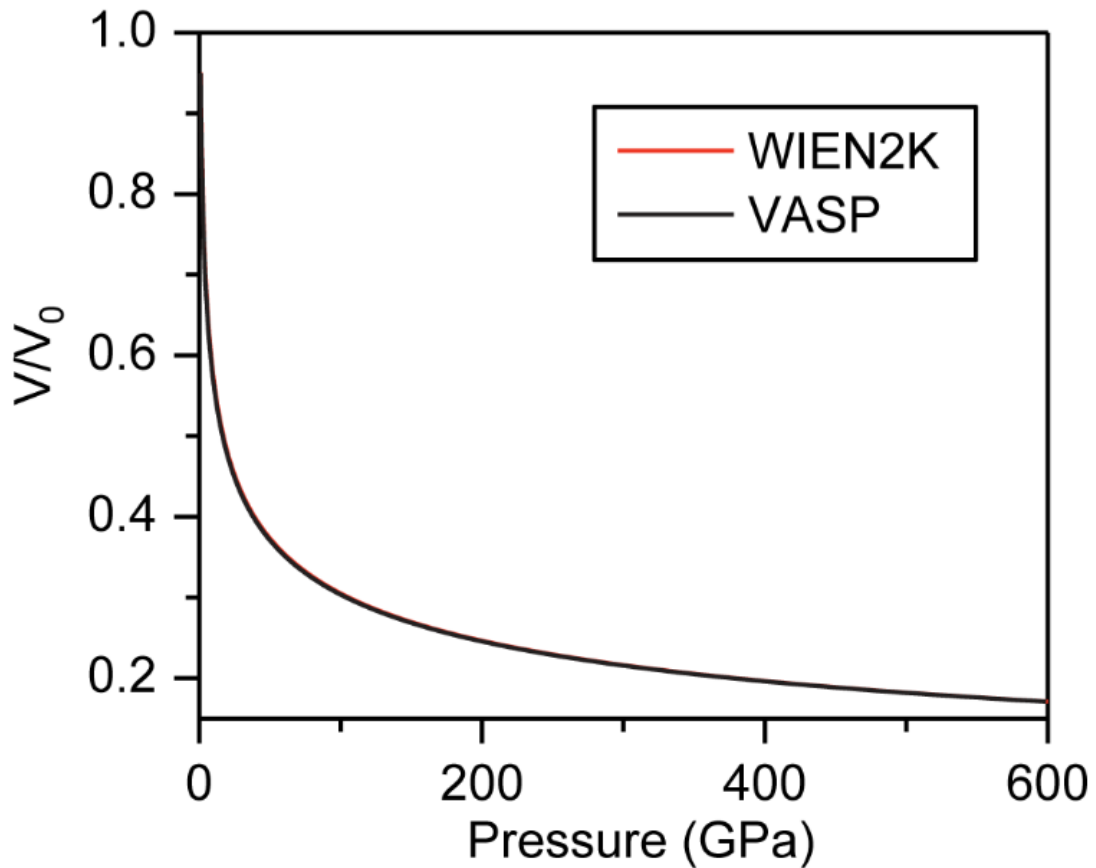
- 37 Perdew, J. P., Burke, K. & Ernzerhof, M. Generalized gradient approximation made simple. *Phys. Rev. Lett.* **77**, 3865-3868 (1996).
- 38 Kresse, G. & Joubert, D. From ultrasoft pseudopotentials to the projector augmented-wave method. *Phys. Rev. B* **59**, 1758-1775 (1999).
- 39 Blaha, P., Schwarz, K., Sorantin, P. & Trickey, S. B. Full-potential, linearized augmented plane wave programs for crystalline systems. *Comput. Phys. Commun.* **59**, 399-415 (1990).
- 40 Togo, A. & Tanaka, I. First principles phonon calculations in materials science. *Scr. Mater.* **108**, 1-5 (2015).
- 41 Parlinski, K., Li, Z. Q. & Kawazoe, Y. First-principles determination of the soft mode in cubic ZrO₂. *Phys. Rev. Lett.* **78**, 4063-4066 (1997).
- 42 Hernández, E. R., Rodríguez-Prieto, A., Bergara, A. & Alfè, D. First-principles simulations of lithium melting: stability of the bcc phase close to melting. *Phys. Rev. Lett.* **104**, 185701 (2010).
- 43 Greenwood, D. The Boltzmann equation in the theory of electrical conduction in metals. *Proc. Phys. Soc.* **71**, 585 (1958).
- 44 Calderín, L., Karasiev, V. V. & Trickey, S. B. Kubo–Greenwood electrical conductivity formulation and implementation for projector augmented wave datasets. *Comput. Phys. Commun.* **221**, 118-142 (2017).
- 45 Giannozzi, P. *et al.* QUANTUM ESPRESSO: a modular and open-source software project for quantum simulations of materials. *J. Phys. Condens. Matter* **21**, 395502 (2009).



Extended Data Fig. 1 | Simulation of mixing 144 atoms of H_2O and 48 atoms of H_2 in a supercell. **a**, Initial construction of the supercell with the H_2O and H_2 components. **b**, A snapshot of the last step of the AIMD simulation at 4.30 g/cm^3 and $7,000 \text{ K}$. The density is chosen so that simulated pressures lie well inside the range of the ice layer in Uranus and Neptune. **c**, Comparison of radial distribution function of the equilibrated H_2 - H_2O mixing and the corresponding result for the H_3O phase described in the main text. The two sets of results appear nearly identical, highlighting the main conclusion that superionic H_2O reacts with H_2 to form H_3O at the conditions of deep-mantle ice layers of Uranus and Neptune.

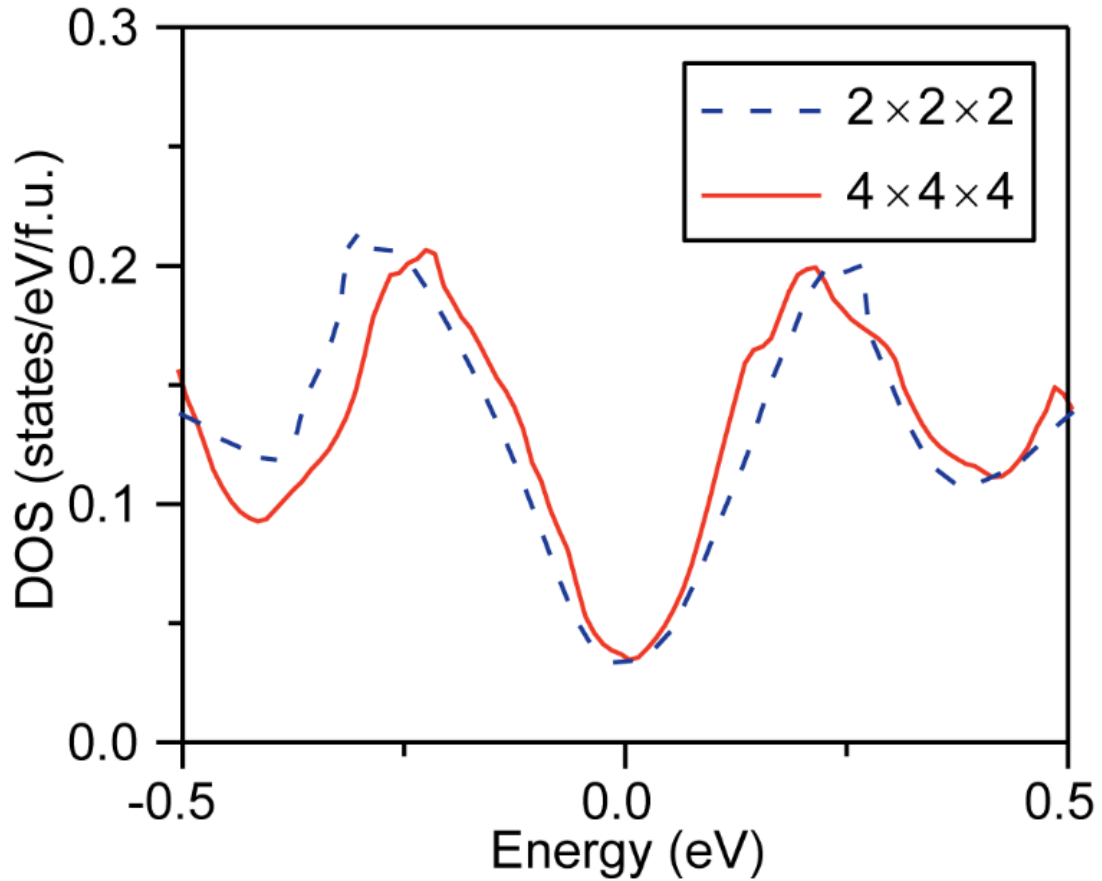


Extended Data Fig. 2 | Metallicity of liquid H₃O. **a**, Evolution of time-averaged bandgap for H₃O (at the density of 4.30 g/cm³, with an equilibrium pressure ~600 GPa at 7,000 K) compared with H₂O (at the density of 4.93 g/cm³, with an equilibrium pressure ~600 GPa at 7,000 K) as a function of temperature obtained by using the GW method that is known to give reliable bandgap values. **b**, Calculated time-averaged direct-current (DC) electrical conductivity for H₃O compared with the results for H₂O as a function of temperature obtained using the Kubo-greenwood formula.

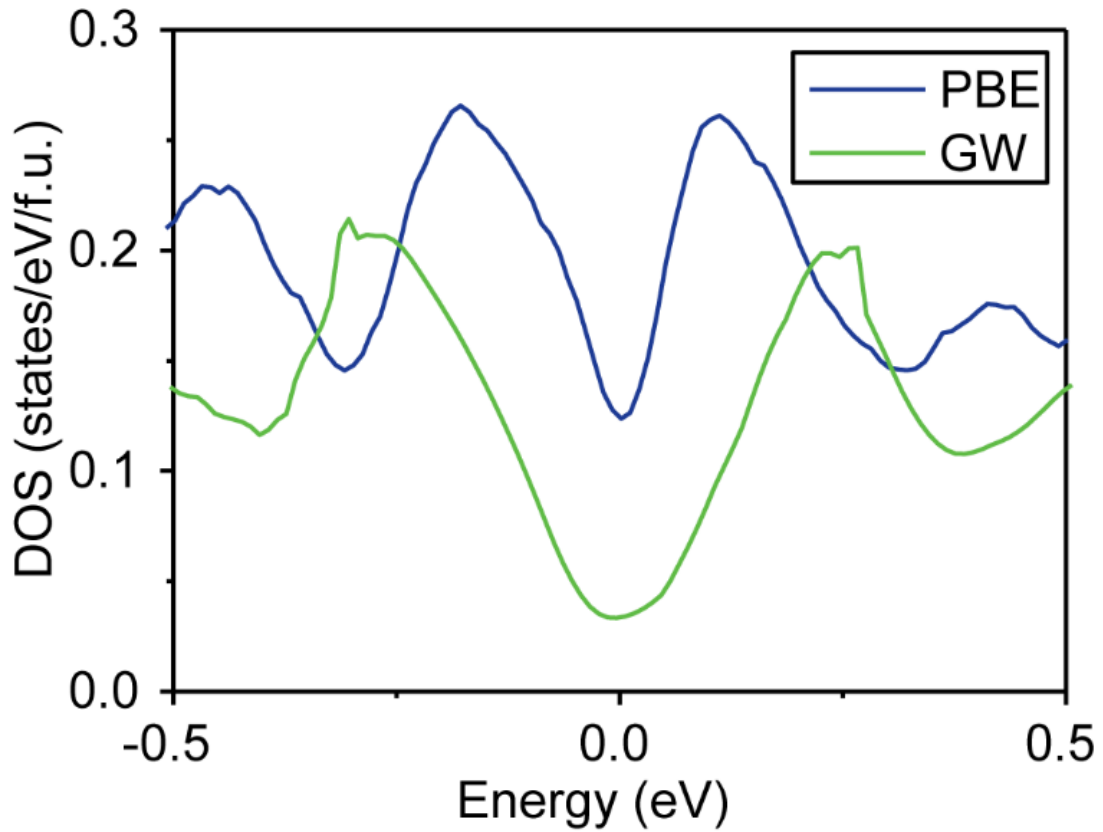


Extended Data Fig. 3 | Equation of states of H₃O calculated by VASP and WIEN2K.

To test the adequacy of the pseudopotentials used in the calculations at high pressures examined in the present work, we have computed the equation of states of H₃O by using the VASP code, which adopts the pseudopotentials, and compared the results against those obtained using the full potential as implemented in the WIEN2K code. Calculated results presented here show that these two computational methods produce nearly identical data, thus validating the pseudopotentials adopted in the VASP calculations over the wide pressure-volume range examined in the present work.



Extended Data Fig. 4 | Convergency test of the time-averaged electronic density of states for H₃O with respect to the k-mesh grid used in the GW calculations. To balance computational efficiency and reliability, we have performed convergency test on k-mesh adopted in the calculations of electronic density of states reported in the present work. The calculations were performed at the density of 4.30 g/cm³, with an equilibrium pressure ~600 GPa at 7,000 K. A comparison of the computed data obtained using a 2×2×2 and a 4×4×4 mesh indicates that the former set of results is well converged, and therefore the 2×2×2 mesh is employed in the calculations of the time-averaged electronic density of states presented in the main text.



Extended Data Fig. 5 | The time-averaged electronic density of states of H₃O at 7,000 K by the PBE-GGA functional and the GW method. Two sets of calculations were performed to examine the reliability and consistency of the results obtained from computations using the PBE functional and the GW method. The calculations were performed at the density of 4.30 g/cm³, with an equilibrium pressure ~600 GPa at 7,000 K. Results presented here show that both methods produce consistent outcome indicating that H₃O is metallic at 7,000 K, despite some quantitative differences in charge distribution, which have no impact on our main conclusions about the key benchmarks on metallicity of H₃O under the physical conditions studied here.